



Ukai, T., Zare-Behtash, H., Kontis, K., Yang, L. and Erdem, E. (2017) Experimental investigation of surface flow pattern on truncated cones in Mach 5 flow: influence of truncation ratio. *Experimental Thermal and Fluid Science*, 81, pp. 396-405. (doi:[10.1016/j.expthermflusci.2016.09.016](https://doi.org/10.1016/j.expthermflusci.2016.09.016))

This is the author's final accepted version.

There may be differences between this version and the published version. You are advised to consult the publisher's version if you wish to cite from it.

<http://eprints.gla.ac.uk/129179/>

Deposited on: 07 October 2016

Enlighten – Research publications by members of the University of Glasgow  
<http://eprints.gla.ac.uk>

# Experimental Investigation of Surface Flow Pattern on Truncated Cones in Mach 5 Flow: Influence of Truncation Ratio

Takahiro Ukai<sup>\*</sup>, Hossein Zare-Behtash, Konstantinos Kontis

*University of Glasgow, School of Engineering, Glasgow, G12 8QQ, UK*

Leichao Yang

*National University of Defence Technology, Changsha, 410073, P.R. China*

Erinc Erdem

*TEI Tusas Engine Industries, Inc., Turkey*

**\*Corresponding author: Takahiro Ukai**

**email:** *Takahiro.Ukai@glasgow.ac.uk*

**Telephone:** + 44-141-330-2477

## Abstract:

The flow characteristics on a truncated cone with a cylinder were experimentally investigated in a Mach 5 flow with a Reynolds number  $3.8 \times 10^5$ , based on the cylindrical diameter. Two different truncation ratios of 0.5 and 0.7 were used. The incidence angle varied from -12 to 0 degrees with 3 degrees intervals to investigate the influence of the truncation ratio on the surface flow pattern. The measurement techniques: unsteady pressure-sensitive paint (anodized aluminium method), colour Schlieren photography, and surface oil flow were used. It was found that the distance of the external shock wave from the conical surface depends on the truncation ratio, and the surface pressure on the conical portion increases when the external shock wave moves closer to the model surface. The "external" shock wave denotes a detached shock wave and the "internal" one is the shock wave formed between the detached bow shock wave and the model surface. In the higher truncation ratio at the higher incidence angle, the internal shock wave induced by the flow separation on the conical surface impinges on the external shock wave, which results in its reflection. This reflection leads to the pressure increase on the model surface. On the other hand, this reflection does not appear in the lower truncation ratio. In spite of the different truncation ratios, the angle of the internal shock wave is identical at the same incidence angle. From the oil flow results, the wall shear stress on the leeward conical surface is larger in the higher truncation ratio model.

**Keywords:** Truncated cone, Pressure-sensitive paint, Hypersonic flow

## 1. Introduction

Investigation into the aerodynamic performances of fundamental and classical geometries, such as cones and cylinders, is important for aerodynamic research. These geometries are often used for high-speed vehicle design since their shapes significantly affect the aerodynamic performances: aerodynamic drag and stability, as well as heat-transfer and sonic-boom propagation. Flow characteristics of cone shapes have been theoretically and experimentally investigated, the model incidence angle has been seen to significantly affect the flow features [1-3]. At higher incidence angles, the flow characteristics such as flow separation, pressure distribution, and boundary layer development become even more complicated [4-7]. Rainbird [8] experimentally investigated the flow features on a yawed cone and showed that flow separation develops on the leeward side at high angles of attack, which results in the generation of symmetrical vortices. Aerodynamic performances must be evaluated at a wide range of incidence angles, and the complete understanding of the flow characteristics is important, in the longer term: for safe, efficient, and environmentally friendly high-speed vehicle design and in the shorter term: for verification and validation of numerical codes.

The truncated cone geometry is utilised for engineering design and fundamental investigation. Pitot-tubes which have a truncated cone shape are designed with consideration about the flow features around them. This is because the cone angle significantly impacts the measurement uncertainty [9] although its geometry as well as the support configuration is also an important geometrical parameter [10]. The truncated cone geometry is a key parameter for drag reduction of projectiles. The drag of the truncated cone is lower than a sharp cone projectile but this effectiveness depends on the Mach number and surface area of the truncated cone [11]. A recent experimental research activity examined a truncated cone model and its drag reduction owing to energy deposition [12]. Having a large truncation diameter exhibited better performance for drag reduction compared to a small one.

The shape of the truncated cone significantly impacts its aerodynamic performance. When supersonic or hypersonic flow passes over a truncated cone, an interesting phenomenon occurs. An expansion fan generated at a nose corner leads to flow separation but the flow reattaches on the conical surface, which results in a reattachment shock wave. The surface pressure in the nose corner region is related to the nose corner radius, and it is found that increasing the nose corner radius results in an alleviated pressure gradient [3]. According to an experimental investigation of the flow characteristics around a truncated cone with various half-cone angles [13], in spite of various half-cone angles, the stand-off distance was identical; however, the half-cone angle influenced to the reattachment shock angle. Although the shape of the nose corner and the cone angle affect the flow characteristics, other geometrical parameters are also key contributors.

Surface pressure measurement techniques are a useful to evaluate the influence of flow conditions and the geometrical parameters on the flow characteristics, moreover surface pressure measurement techniques enable an in-depth understanding of them. Brodetsky *et al.* [13] investigated the surface pressure on a truncated cone using a static pressure tapping. Although the flow characteristics at wide range of Mach numbers for the truncated cone model was investigated, the low surface pressure due to flow separation at the nose corner was not captured because a point pressure measurement was employed. Pressure-sensitive paint (PSP), which is a surface pressure measurement technique, has the ability to capture the detailed pressure distribution [14-20]. The anodized aluminium pressure-sensitive paint (AA-PSP) techniques which has a high response time is useful for the application in unsteady and high-speed flow fields, and the successful application of AA-PSP has been reported at various Mach numbers [14-27]. Yang *et al.* [27] applied the AA-PSP technique to surface pressure measurement on a truncated cone in hypersonic flow and captured the in-depth flow characteristics.

This study focuses on the investigation into the influence of truncation ratio and incidence angles on the flow field. Two truncated cone models with different truncation ratios of 0.5 and 0.7 were studied. The model incidence angle was varied from -12 to 0 degrees with 3 degrees intervals. The experiments were conducted in a Mach 5 flow with a Reynolds number of  $3.8 \times 10^5$  based on the cylindrical diameter. The flow diagnostics techniques: AA-PSP, colour Schlieren, infrared thermograph, and surface oil flow were used.

## **2. Experimental setup**

### **2.1 Wind tunnel facility and test models**

The experimental investigation was conducted in a high supersonic wind tunnel in the University of Manchester. The wind tunnel is an intermediate blow-down wind tunnel with test duration time up to 7.5 seconds, which depends on the vacuum and supply pressure conditions. Air from a high pressure gas supply is dried and stored in a pressure reservoir at 1.6 MPa. After passing through a pneumatically operated quick-acting ball valve, the dried air enters into an electrical heater which heats the air up to 700 K to avoid potential condensation inside the test section. On leaving the heater, the dry air goes through a settling chamber and expands in a nozzle flowing to the test section. In the present experiments, a Mach 5 nozzle with 152 mm diameter exit was used. The tunnel test section is a free-jet type with dimension of 325 mm  $\times$  325 mm  $\times$  900 mm (height  $\times$  width  $\times$  length), and a Quartz window pair 195 mm in diameter on both sides of the test section enable optical access for flow visualisation. A unit Reynolds number of  $4.5 \times 10^6$  to  $16.5 \times 10^6$  m<sup>-1</sup> can be obtained by the supply pressure and heater temperature setting. At the present experimental condition, the unit Reynolds

number is  $12.9 \times 10^6 \text{ m}^{-1}$ . The wind tunnel was calibrated and the variation of Mach number and unit Reynolds number were found to be  $\pm 0.4\%$  and  $\pm 3.5\%$ , respectively. A schematic sketch of the wind tunnel facility is presented in [28]. A sting mounted on an arc arm in the test section allows for the change in the pitching angle of the model. The incidence angle can be varied from -20 to 20 degrees. Further detail of the facility and measurement instruments are reported by Erdem [28, 29].

Two truncated cones with different truncation ratios were used in the present experiment. The model is a 15 degrees semi-apex cone followed by a 35 mm cylinder with 30 mm diameter. The Reynolds number based on the cylindrical diameter is  $3.8 \times 10^5$ . The cone nose is truncated by removing the lengths of 29 and 43.5 mm from the nose tip. Thus, the truncation ratios, defined here as the truncated diameter to the cylinder diameter, are 0.5 and 0.7 for the two models, respectively (Fig. 1). The truncated cone models were mounted on the sting inside the test section. The incidence angle is varied from -12 to 0 degrees with 3 degrees intervals relative to the freestream direction. The wind tunnel flow conditions are summarised in Table 1. For the surface pressure measurement, the conical and cylindrical surfaces were coated with AA-PSP. A uniform porous layer was created on the model surface according to anodization procedure of Sakaue [30]. More details regarding the anodization process can be found in references [31, 32]. The anodized model is dipped into the PSP solution with a concentration of  $0.3 \times 10^{-3} \text{ mol/L}$  as suggested by Gregory *et al.* [14].

## 2.2 Pressure-sensitive paint technique

The AA-PSP was excited by a pair of continuous LED panels with peak wavelength of 470 nm. The LED panel was placed on each side of test section and provided uniform illumination to the test model. The AA-PSP system has been successfully applied to various models in a Mach 5 flow [33, 34]. A 12-bit LaVision Image intense charge-coupled device (CCD) camera was used to acquire the fluorescent emission. The LED light source is found very stable and the intensity variation is less than  $\pm 5\%$ . Therefore, the effect of illumination variation can be neglected in the current experiment. A combination of 550 nm long pass and infrared rejection filter was placed in front of the camera to separate the emission from excitation light. The CCD camera was then connected to a PC for image acquisition and operated at 10 ms exposure time with 9 fps frame rate.

A-priori calibration of the PSP was conducted in the test section where the pressure can be controlled. The fluorescence emission signal was recorded at each known pressure. A-priori calibration can be obtained by plotting the intensity as a function of pressure. A dark image was recorded and then subtracted from the raw test image for dark compensation. Immediately after each test, a reference PSP image was recorded at a known pressure used as reference image. The PSP test images were acquired after stable flow was reached, and a total of 30 test images were averaged. The stable flow was

established 0.5 seconds after wind tunnel start. The intensity ratio of the PSP images was obtained by dividing the testing intensity of a raw image to the corresponding reference image, after the two images were fitted to pixel-to-pixel, because of the minor movement of the test model during the test run. The a-priori calibration curve was utilised to convert the intensity ratio to a pressure distribution.

The PSP measurement accuracy due to the temperature dependency was found to be insignificant in the present experiment. To evaluate the effect of the temperature change on the surface pressure measurement, the model temperature distribution was recorded by an IR camera (FLIR ThermoCAM SC 3000, temperature range of -20 to 2000 °C with an accuracy of  $\pm 1\%$ , spectral range of 8 to 9  $\mu\text{m}$ ) set at a frame rate of 50 fps. The camera was placed on top of the test section and visualised the model surface through a Germanium window coated at 3 to 12  $\mu\text{m}$ . Figure 2 shows the surface temperature of cone 1 on the windward side at -12 degrees incidence angle which is the most critical incidence angle for the temperature increase. The time evolution of the temperature profiles at the different measurement locations are also shown in Fig. 2. Generally, at the beginning, the model is at room temperature, and the model temperature increases during the test duration. The highest temperature occurs at the nose corner of the model while lower temperature appears on the cylindrical surface. The temperature increase is observed to be less than 5 °C on the conical portion and less than 2 °C on the cylindrical portion with respect to an initial temperature. This initial temperature is almost the same as the temperature in the a-priori calibration. The PSP test images are averaged between approximately 0.5 and 3.8 seconds, and the surface temperature difference between the conical and cylindrical surfaces was less than 3 °C at this time range. When the worst case is now taken into account, the maximum temperature difference is approximately 4.5 °C which appears near the model nose corner at a range of 0 to 3.8 seconds test duration. Quinn *et al.* [18] measured the temperature sensitivity of the present AA-PSP substrate and calculated a temperature dependency - 0.64% / °C. The maximum normalized pressure is  $P/P_\infty = 10.5$  which corresponds to the maximum surface pressure  $P = 12.8$  kPa. The maximum uncertainty of local pressure due to the temperature dependency is 2.9% which corresponds to a maximum pressure error of  $\pm 0.19$  kPa.

### 2.3 Flow visualisation techniques

A colour Schlieren photography with a standard Z-type optical arrangement was employed for flow visualisation of the density field. A pair of 203 mm diameter parabolic mirrors with 1829 mm focal length, and a high intensity illuminance light source, Palfsh 501 (Pulse Photonics) were used. A parallel light beam collimated by the first parabolic mirror passes through the test section. Then, the parallel beam is focused by the second parabolic mirror. The optical arrangement has been successfully applied in previous studies [35, 36]. A tricolour filter containing three parallel colour strips was put at the focal

position of the second parabolic mirror [37]. A digital Canon SLR camera was set in continuous shooting mode at 3.5 fps with an exposure time of 0.25 ms.

The oil flow technique was used for surface flow visualisation. The oil mixture used is composed of silicone oil, linseed oil, titanium dioxide, oleic acid, and luminescent dye. The oil streaks left behind by the air flow give an accurate impression of the flow direction. The direction of the oil movement is believed to depend on the wall shear stress and the pressure gradient. The oil flow technique is very useful for indicating flow features such as transition, flow separation, and re-attachment. The current recipe has been used and found to be the optimum for the current test conditions [27]. A 0.5 mm oil dot was placed on a  $5 \times 5$  mm matrix drawn on the model surface before the tests.

### 3. Results and discussions

#### 3.1 External flow structures

The surface pressure map is combined with the colour Schlieren image, figure 3 shows their sideview at the representative incidence angles. The combined images show the external flow structures as well as the surface flow pattern simultaneously, which provides the opportunity for a deeper understanding of the flow phenomenon. A highly curved detached bow shock wave is formed in front of the model nose as the hypersonic flow passes the truncated cone. An expansion fan is generated at the model nose corner, which is the blue colour region at the nose corner shown in Fig. 3. The expansion fan spreads to the front surface. An internal shock wave can be seen generated beyond the nose corner. The generation of this internal shock wave is due to the flow reattachment on the conical surface. An expansion wave is generated at the corner between the conical and cylindrical portions.

The size of the expansion fan generated at the nose corner on the leeward conical surface depends on the surface pressure. The expansion zone on the leeward side increases as the incidence angle is decreased. The leeward surface pressures of cone 2 are  $P/P_\infty = 1.9, 2.0,$  and  $2.3$  at  $0, -6,$  and  $-12$  incidence angles, respectively. These surface pressures are obtained at 1.3 mm from the nose corner. Additionally, the size of the leeward expansion fan of cone 2 is found to be larger than that of cone 1. The expansion fan leads to flow separation that is related to the conical surface pressure. As shown in Figs. 3 (c) and (f), the surface pressure distribution of cone 1 near the nose corner on the leeward side is different from that of cone 2. The leeward surface pressure of cone 2 is  $P/P_\infty = 2.3$  at 1.3 mm from the nose corner, whereas it is  $P/P_\infty = 1.4$  in cone 1. The higher pressure leads the flow separating more readily, and it might be related to the large expansion fan.

The incidence angle and the truncation ratio do not affect the shock wave stand-off distance that we defined as the bow shock distance from the nose surface along the model centre line. The distance

between the bow shock wave and the model surface, known as shock stand-off distance, is an important parameter in describing the detached shock wave. The shock wave stand-off distances for the different incidence angles are measured from the Schlieren photographs with a resolution of  $\pm 0.1$  mm. The stand-off distances measured along the model centre line are normalized with the nose diameter. For all the incidence angles for cones 1 and 2, the normalized stand-off distance was approximately  $0.26 \pm 0.01$ . No relationship between truncation ratio and stand-off distance has been observed, since the measured stand-off distances are almost identical.

The normalized stand-off distance along the model centre line is independent of the incidence angle; however, the incidence angle affects the formation in the bow shock wave. Figure 4 shows the normalized bow shock distances of the windward and leeward sides at the various incidence angles. These distances are measured from the leeward and windward nose corners along the longitudinal axis of the model, and they are normalized with the nose diameter. At 0 degree incidence angle, the normalized bow shock distance on the windward side are the same as the leeward side. When the incidence angle is decreased, the bow shock wave moves closer to the model surface on the windward side, whereas it moves away from the leeward side. As presented in Fig. 4, the normalized bow shock distances are in proportion with the incidence angle. In comparison with the normalized distances of cone 1 and 2, they are almost identical at each incidence angle. However, the normalized shock distance on the conical surface slightly differs at 0 degree incidence angle. The shock distance of the external shock wave was measured along the perpendicular direction to the conical surface. The shock distances normalized with the nose diameter are shown in Fig. 5. The horizontal axis  $L$  means the location on the conical surface, and the position of the model nose corner is defined as  $L = 0$ . The symbol "IA" refers to the incidence angle. The estimated error is approximately  $\pm 0.01$ . The normalized shock distance of cone 1 differs with cone 2 at  $IA = 0$ , whereas they are almost identical at  $IA = -12$ . The external shock wave moves towards the conical surface at  $IA = -12$  but it moves away from the conical surface at  $IA = 0$ ; therefore, the effect of interaction with the external shock wave and the model is larger at  $IA = -12$ . It seems that normalization of the shock distance on the conical surface at the lower incidence angle is not an important parameter in the present experimental result.

Figure 6 shows the distance between the shock waves and the conical surface at  $AI = 0$  and  $-12$  on the windward side. The solid and dashed lines denote the external shock wave (ES) and the internal shock wave (IS), respectively. The same coloured lines correspond to the same cone models and the incidence angles (IA). The distance of the external shock wave depends on the truncation ratio. In cone 2, which has the higher truncation ratio, the external shock wave stands further away from the model surface compared to cone 1 even when the incidence angle is identical. An interesting observation is that as long as the internal shock wave does not interact with the external one, the distance between

the internal shock wave and the model is the same for both truncation ratios at the same incidence angles. It appears that despite the difference in the truncation ratio, the Mach number at the model nose corner is the same for identical incidence angles, and this results in the same angle of the internal shock wave from the model surface.

Shock-shock interaction occurs on cone 1 at IA = -12 (Fig. 3(c)). When the incidence angle decreases, the distance between the external shock wave and the conical surface shortens. Additionally, as shown in Fig. 6, the oblique internal shock wave at AI = 0 changes to a curved one at IA = -12. As a result, the internal shock wave, which is curved, moves closer to the external shock wave. Therefore, the internal shock wave impinges on the external shock wave, and then the reflected internal shock wave is formed on the windward side (Fig. 3 (c)). The reflected internal shock wave leads to the model surface pressure change, which will be discussed later. In comparison with cone 2, the internal shock wave does not interact with the external shock wave (Fig. 3 (f)) because of the greater distance between the external shock wave and the model surface than that of cone 1.

### 3.2 Surface pressure distribution

Analysis of the surface pressure distribution enables a deeper understanding of the surface flow pattern. The surface pressure contour is processed and compared with both truncated cones in Fig. 3. The surface pressure is normalized with the freestream pressure. The red and blue colours indicate the high and low pressures, respectively. Higher pressure is encountered on the conical portion. At IA = 0, the pressure shows a symmetrical pattern on the model surface. Moreover, the flow is attached to the model surface with the exception of the region close to the model nose. This is because the surface pressure near the model nose increases due to the flow reattachment.

It is believed that the distance of the external shock wave from the conical surface directly influences the surface pressure on the conical portion of the model. The greater distance between the external shock wave and the conical surface leads to the lower surface pressure at the same incidence angle. Figure 7 shows the relationship between the distance of the external shock wave and the surface pressure distribution. The dashed line denotes the pressure distribution on the conical surface taken at a circumferential angle of 30 degrees from the model edge on the windward side (the sketch in Fig. 7). For the same truncation ratio, the maximum surface pressure moves closer to the model leading edge when the incidence angle decreases. When the external shock wave is close to the conical surface (cone 2, IA = -12), a higher surface pressure is observed, whereas the distant external shock wave from the conical surface leads to a surface pressure decrease. Figure 8 shows the relationship between the maximum surface pressure on the windward conical portion and the location of the external shock wave. This distance is measured at the conical portion where the maximum surface pressure appears

between  $L = 0$  to 10 mm. The surface pressure generated at more than  $L = 10$  mm is not included in the measurements because it is affected by the reflected internal shock wave. For both truncation ratios at all incidences, the maximum surface pressure increase is proportional to the reduction of the distance of the external shock wave from the model surface. On the other hand, the internal shock wave does not strongly affect the conical surface pressure unless a reflected shock wave is generated (see Fig. 9). In cones 1 and 2 at  $IA = 0$ , the internal shock waves are identical in shape; however the surface pressures are different. In case of the same truncation ratio, the internal shock wave close to the model surface leads to the surface pressure increase; however, it can be expected that the effect of the internal shock on the surface pressure is weak in the present Mach number. According to a previous study [3], the expansion fan at the nose corner of the truncated cone becomes weak at high Mach numbers. Note that the expansion fan at the nose corner is related to the internal shock wave.

When the internal shock wave impinges on the external shock wave, the surface pressure is dramatically changed by the reflected internal shock wave. An interesting phenomenon is that the conical surface pressure changes in shape. For cone 1 at  $IA = -12$  (Fig. 3 (c)), a complicated “hourglass” shape occurs on the conical surface. At the conical surface over a range of  $L = 5$  to 10 mm in Fig. 9, the gradient of the surface pressure distribution on cone 1 at  $IA = -12$  is similar to that of cone 2, although the shape of the pressure distribution differs at the range of 0 to 5 mm due to the large effect of flow separation near the nose tip. The conical surface pressure gradually decreases towards the aft conical surface; however, the surface pressure on cone 1 increases at  $L = 13$  mm because the reflected internal shock wave is generated at this location. Moreover, the reflected internal shock wave impinges on the expansion wave, generated from the corner between the conical and cylindrical portions, thus, the surface pressure on the cylindrical portion is larger than that of cone 2 (see Fig. 3 (c) and (f)). On the other hand, the “hourglass” feature does not occur on the conical surface of cone 2 because the internal shock wave does not reflect from the external shock wave.

When the incidence angle is decreased, a curved pressure pattern on the side of the conical surface was formed (see Fig. 3 (b, c, e and f)). Additionally, a sloped pressure pattern appeared on the cylindrical surface on the windward side. These formations are believed to be linked to the three-dimensional shape of the shock wave. A schematic of the three-dimensional flow field at  $IA = -12$  is shown in Fig. 10. The effect of the reflected internal shock wave is due to the three-dimensional flow. In cone 1, the size of the area where the surface pressure range of  $P/P_\infty = 3.5$  to 7 occurs on the cylindrical portion is larger than that of cone 2. This pressure increase on the cylindrical surface is caused by the impingement of the reflected internal shock wave; however, the surface pressure decreases on the conical surface. This is because the reflected shock wave disappears at position  $T$  shown in Fig. 10 (a) due to the three-dimensional effect. On the other hand, in cone 2, the surface

pressure only slightly changes on the cylindrical portion. Although the internal shock wave does not reflect, it slightly impinges on the external shock wave above the corner between the conical and cylindrical portions; thus, it results in the slight pressure increase however the pressure increase zone is smaller than that of cone 1. The three-dimensional shock wave strongly influences the surface pressure distribution and leads to the curved pressure pattern on the side of the conical surface. The external shock wave on the leeward side stands further away from the model surface, and moves closer to the model surface on the windward side; i.e., the external shock wave gradually moves away from the model surface toward the leeward side. The surface pressure change greatly depends on these distances.

Although the size of the curved pattern is different between cones 1 and 2, it seems that this size is related to the truncated length. Figure 11 shows the pressure distribution along the circumferential coordinate on the conical surface at the various incidence angles. As presented in Fig. 11 (a), the circumferential angle ( $\beta$ ) starts from the windward side to the leeward side. The solid and dashed lines denote the pressure distributions of cones 1 and 2, respectively. To evaluate the pressure change on the different truncation ratio, the pressure subtracted from the pressure at IA = 0 is used. This subtracted pressure:  $(P/P_\infty) - (P/P_\infty)_{AoA=0}$  shown in Fig. 11 is obtained at a normalized distance from the nose corner. The subscript “AoA 0” denotes the 0 degree incidence angle. The normalized distance by the truncated length of cone is defined as  $L/t$ , and  $L/t = 1/10, 1/5, \text{ and } 1/2$  are used. As shown in Fig. 11, the pressure peaks appear at a range of  $\beta = 30$  to 40 degrees since insufficient fluorescent emission is captured at  $\beta \leq 20$  degrees. The peak surface pressure is slightly altered due to the positional relation between the LED light, the camera, and the model. For the same incidence angle and the normalized distance, the gradient of the pressure distribution on cone 1 resembles that of cone 2, although both curved pressure patterns shown in Fig. 3 (c) and (f) are different in size. At IA = -6, the subtracted pressure magnitude of cone 1 is the same as cone 2; however, the magnitude of this difference increases in proportion to the incidence angle decrease (at IA = -9 and -12) with the exception of  $L/t = 1/10$  which is near the nose corner. This is because the surface pressure on the middle portion on the conical surface is slightly affected by the reflected shock wave when the incidence angle decreases.

The circumferential surface pressure distribution that decreases towards the leeward side resembles that of a sharp cone. However, the surface pressures on the sharp cone at the various incidence angles become the same pressure at the circumferential angle of approximately 80 degrees [38, 39], whereas the surface pressure on the truncated cone is similar at approximately 90 degrees. This difference of the circumferential angle might be induced by more complicated three-dimensional flows around the truncated cone because the flow is separated and reattached around the nose corner.

### 3.3 Surface flow pattern

The oil mixture follows the surface flow, leaving streaks which indicate the flow direction. The direction and the length of the oil dot movement depend on the local wall shear stress and pressure gradient. This is a very useful technique to show the crossflow and regions of high pressure gradients such as flow separation and reattachment. Figures 12 and 13 present the oil dot results on the truncated cone surfaces at  $IA = 0$  and  $-12$  on the leeward (top), windward (middle), and side (bottom) views.

The oil flow results qualitatively match the pressure distributions measured by AA-PSP, where the oil dot movement matches the direction of the pressure gradient. At  $IA = 0$ , the oil dot movement is uniform and moves parallel with the freestream towards the downstream direction. There is no sign of crossflow in all of the views. The oil dot movement becomes more distinguished at  $IA = -12$ . At  $IA = -12$ , flow separation on the leeward side close to the model nose starts to grow, where the oil streak length is shorter than the surrounding areas because the flow is decelerated. Figure 14 shows the oil streak length along approximately  $\beta = 180$  degrees on the leeward conical surface at  $IA = -12$ .  $l$  denotes the oil streak length, and the location of  $\beta$  is shown in Figs 12 and 13. The streak length, which is indicative of the wall shear stress, gradually increases from the nose edge to the aft conical portion. The flow direction on the surface causes change in the oil streak length. As show in the side view at  $IA = -12$  (Figs. 12 and 13), the oil streaks move from the windward side to the leeward side. From the oil streak direction at  $IA = -12$  on the leeward view, the oil streaks arranged on the circumference are almost parallel on the conical surface close to the nose corner, whereas the later oil streaks move towards the model centre line ( $\beta = 180$  degrees). As a result, the surrounding flow moves towards the leeward aft conical surface, and it might increase the wall share stress on this region. When comparing the streak lengths of cone 1 with cone 2 in Fig. 14, the streak length of cone 2 is shorter than that of cone 1, which indicates that the wall shear stress is larger on cone 1. In cone 1, the flow easily comes from the windward to leeward compared with cone 2 because of the small nose face.

Figure 15 shows the oil streak length on the leeward cylindrical surface.  $L_{cy}$  denotes the length on the cylindrical surface, and  $L_{cy} = 0$  is defined as the corner between the conical and cylindrical portions. The dashed line denotes a quadratic approximation. The oil streak length along approximately  $\beta = 180$  degrees is shown in Fig. 15 (a). The minimum streak length may refer to the flow separation point. In cone 2, the flow might be separated at approximately 7 mm from the corner on the cylindrical surface, whereas the separation point of cone 1 is approximately 11 mm. In the oil streak length along approximately  $\beta = 150$  degrees (Fig. 15 (b)), they can be compared with the PSP results. The average pressure along approximately  $\beta = 150$  degrees of cone 1 and cone 2 are  $P/P_\infty = 0.9$  and 2.0, respectively. As shown in Fig. 15 and the PSP results, it can be deduced that the wall shear stress of cone 1 is larger

than that of cone 2.

#### **4. Conclusion**

An experimental investigation about the flow over a truncated cone with different truncation ratios was performed in a Mach 5 flow. The model incidence angle was varied from -12 to 0 degrees relative to the freestream direction at 3 degrees intervals to study the influence of the incidence angle and the truncation ratio on the external flow structures and the surface flow pattern. Pressure-sensitive paint, colour Schlieren, and oil dot flow visualisation were used to understand the flow patterns and surface pressure distribution at the various incidence angles.

The normalized bow shock distances along the longitudinal axis of the leeward and windward model nose corner depends on the incidence angle. In comparison with the normalized bow shock distances of both the truncation ratios, they are almost identical at each incidence angle. The distance of an external shock wave (detached shock wave) from the conical surface was found to be dependent on the truncation ratio, and the surface pressure on the conical portion increased when the external shock wave moved closer to the model surface. An internal shock wave was formed because of the flow reattachment on the conical surface. When the incidence angle decreases, a reflected internal shock wave was formed in the higher truncation ratio model, which results in a surface pressure increase on the aft conical portion. In spite of the different truncation ratios, the internal shock wave did not alter the pressure on the conical surface unless the reflected internal shock wave is generated. The reflected internal shock wave leads to a pressure increase on the cylindrical surface because the expansion wave generated from the corner between the conical and cylindrical portions is attenuated. The surface pressure increase due to the reflected internal shock wave is strongly related to the three-dimensional flow. The reflected internal shock wave disappears on the model side surface because the external shock wave which causes the reflection moves away from the model surface towards the leeward side. A curved pressure pattern was formed on the fore conical surface due to a three-dimensional effect, and it seems that its pressure pattern relates to a truncated length. The flow separation location was detected by the oil flow results. On the leeward conical surface, the wall shear stress gradually increased from the nose edge to the aft conical portion. In comparison with different truncation ratios, the wall shear stress should be larger in the higher truncation ratio model. On the leeward cylindrical surface of lower truncation ratio, the flow is expected to separated earlier near the fore cylindrical surface compared with higher one.

## Acknowledgments

We would like to dedicate this paper to Mr. Adrian Walker and all the staff at the EPSRC Instruments Loan Pool for their many years of hard work and support with the various equipment, to which many researchers owe their results, publications, and Ph.Ds.

## References

- [1] Alhussan, K., “Computational analysis of high speed flow over a conical surface with changing the angle of attack,” *Procedia Engineering* 61, 48-51, 2013.
- [2] Willett, J.E., “Supersonic flow at the surface of a circular cone at angle of attack,” *Journal of Aerospace Sciences* 27 (12), 907-912, 1960.
- [3] The Johns Hopkins University Applied Physics Laboratory, “Handbook of supersonic aerodynamics,” Navweps report vol. 3, section 8, 1488.
- [4] Lin, T.C., Rubin, S.G., “Viscous flow over a cone at moderate incidence. Part 2. Supersonic boundary layer,” *Journal of Fluid Mechanics* 59, 593-620, 1973.
- [5] Fletcher, C.A.J., Holt, M., “Supersonic viscous flow over cones at large angles of attack,” *J. Fluid Mech.* 74 (3), 561-591, 1976.
- [6] Nebbeling, C., Bannink, W.J., “Experimental investigation of the supersonic flow past a slender cone at high incidence,” *J. Fluid Mech.* 87 (3), 475-496, 1978.
- [7] Adams Jr.J.C., Three-dimensional compressible turbulent boundary layer on a sharp cone at

- incidence in supersonic flow,” *International Journal of Heat and Mass Transfer* 17, 581-593, 1974.
- [8] Rainbird, W.J., “Turbulent boundary-layer growth and separation on a yawed cone,” *AIAA Journal* 6, 2410-2416, 1968.
- [9] Maddalena, L., Hosder, S., Bonanos, A.M., Dimotakis, P.E., “Extended conical flow theory for design of pressure probes in supersonic flows with moderate flow angularity and swirl,” AIAA paper, AIAA 2009-1072, 2009.
- [10] Allen, J.M., “Influence of probe geometry on pitot-probe displacement in supersonic turbulent flow,” *AIAA journal* 13 (7), 949-950, 1975.
- [11] Charters, A.C., Stein, H., “The drag of projectiles with truncated cone headshapes,” Ballistic research laboratory, report No. 624, 1951.
- [12] Sasoh, A., Kim, J.-H., Yamashita, K., Sakai, T., “Supersonic aerodynamic performance of truncated cones with repetitive laser pulse energy deposition,” *Shock wave* 24, 59-67, 2014.
- [13] Brodetsky, M.D., Shevchenko, A.M., “Experimental study of supersonic flow around truncated cones at incidence,” *Journal of Applied Mechanics and Technical Physics* 44, 640-647, 2003.
- [14] Gregory, J.W., Asai, K., Kameda, M., Liu, T., Sullivan, J.P., “A review of pressure-sensitive paint for high-speed and unsteady aerodynamics,” *Proceedings of the Institution of Mechanical Engineering, Part G: Journal of Aerospace Engineering* 222, 249-290, 2008.
- [15] Kontis, K., “A review of some current research on pressure sensitive paint and thermographic phosphor techniques,” *The Aeronautical Journal*, paper No. 3162, 495-508, (2007).
- [16] Kontis, K., Lada, C., Zare-Behtash, H., “Effect of dimples on glancing shock wave turbulent boundary layer interactions,” *Shock Wave* 17, 323-335, 2008.
- [17] Gongora-Orozco, N., Zare-Behtash, H., Kontis, K., “Effects of filters on the performance and characteristics of pressure-sensitive paints,” *Measurement Science and Technology* 20, 077004, 2009.
- [18] Quinn, M.K., Yang, L., Kontis, K., “Pressure-Sensitive Paint: Effect of Substrate,” *Sensors* 11, 11649-11663, 2011.
- [19] Zare-Behtash, H., Gongora-Orozco, N., Kontis, K., Holder, S.J., “Application of novel pressure-sensitive paint formulations for the surface flow mapping of high-speed jets,” *Experimental Thermal and Fluid Science* 33, 852-864, 2009.
- [20] Gongora-Orozco, N., Zare-Behtash, H., Kontis, K., “Global unsteady pressure-sensitive paint measurements of a moving shock wave using thin-layer chromatography,” *Measurement* 43, 152-155, 2010.
- [21] Kameda, M., Tabei, T., Nakakita, K., Sakaue, H., Asai, K., “Image measurements of unsteady

- pressure fluctuation by a pressure-sensitive coating on porous anodized aluminium,” *Measurement Science and Technology* 16, 2517-2524, 2005.
- [22] Sakamura, Y., Matsumoto, M., Suzuki, T., “High frame-rate imaging of surface pressure distribution using a porous pressure-sensitive paint,” *Measurement Science and Technology* 16, 759-765, 2005.
- [23] Sakaue, H., “Porous pressure-sensitive paint for characterizing unsteady flowfields,” *AIAA Journal* 40, 1094-1098, 2002.
- [24] Nakakita, K., Yamazaki, T., Asai, K., Teduka, N., Fuji, A., Kameda, M., “Pressure sensitive paint measurement in a hypersonic shock tunnel,” AIAA paper, AIAA-2000-2523, 2000.
- [25] Nakakita, K., Asai, K., “Pressure-sensitive paint application to a wing-body model in a hypersonic shock tunnel,” AIAA paper, AIAA-2002-2911, 2002.
- [26] Yang, L., Zare-Behtash, H., Erdem, E., Kontis, K., “Application of AA-PSP to hypersonic flows: the double ramp model,” *Sensors and Actuators B: Chemical* 161, pp. 100-107, 2012.
- [27] Yang, L., Erdem E., Zare-Behtash, H., Kontis, K., Saravanan, S., “Pressure-sensitive paint on a truncated cone in hypersonic flow at incidences,” *International Journal of Heat and Fluid Flow* 37 (2012) 9–21
- [28] Erdem, E., Kontis, k., “Numerical and experimental investigation of transverse injection flows,” *Shock Wave* 20, 103-118, 2010.
- [29] Erdem, E., Kontis, K., Yang, L., “Steady energy deposition at Mach 5 for drag reduction,” *Shock wave* 23 (84) 258-1264, 2013.
- [30] Sakaue, H., “Luminohpore application method of anodized aluminium pressure sensitive paint as a fast responding global pressure sensor,” *Review of Scientific Instruments* 76, 1-6, 2005.
- [31] Sakaue, H., Sullivan, J.P., “Time response of anodized aluminum pressure-sensitive paint,” *AIAA Journal* 39, 1944-1949, 2001.
- [32] Kameda, M., Tezuka, N., Hangai, T., Asai, K., Nakakita, K., Amao, Y., “Adsorptive pressure-sensitive coatings on porous anodized aluminium,” *Measurement Science and Technology* 15, 489-500, 2004.
- [33] Yang, L., Erdem E., Kontis, K., “Pressure-sensitive paint application on two dimensional and axisymmetric model in hypersonic flow,” AIAA paper, AIAA-2011-849, 2011.
- [34] Yang, L., Zare-Behtash, H., Erdem, E., Kontis, K., “Investigation of the double ramp in hypersonic flow using luminescent measurement systems,” *Experimental Thermal and Fluid Science* 40, 50-56, 2012.
- [35] Bradley, J.W., Oh, J.S., Olumuyiwa, T., Hale, O.C., Mariani, R., Kontis, K., “Schlieren Photography of the Outflow From a Plasma Jet,” *IEEE Transactions on Plasma Science* 39 (11),

2312-2313, 2011.

- [36] Zare-Behtash, H., Kontis, K., Gongora-Orozco, N., Takayama, K., “Compressible vortex loops: effect of nozzle geometry,” *International Journal of Heat and Fluid Flow* 30, 561-576, 2009.
- [37] Ukai, T., Zare-Behtash, H., Erdem, E., Lo, K.H., Kontis, K., 2014. Effectiveness of jet location on mixing characteristics inside a cavity in supersonic flow. *Experimental Thermal and Fluid Science* 54, 59-67, 2014.
- [38] Yahalom, R., “An experimental investigation of supersonic flow past yawed cones,” Aeronautical Sciences Division University of California Berkeley, Report No. AS-71-2, 1971.
- [39] Collingbourne, J.R., Crabtree, L.F., Bartlett, W.J., “A semi-empirical prediction method for pressures on the windward surface of circular cones at incidence at high supersonic and hypersonic speeds ( $M \geq 3$ ),” London: HER Majesty’s stationery office, C.P. No. 792, 1964.

## Figures

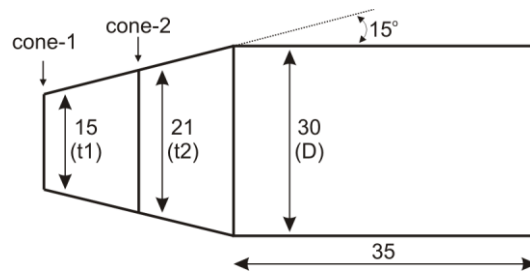


FIG. 1: Schematic of the two truncated cones, where  $t_1/D = 0.5$  and  $t_2/D = 0.7$ .

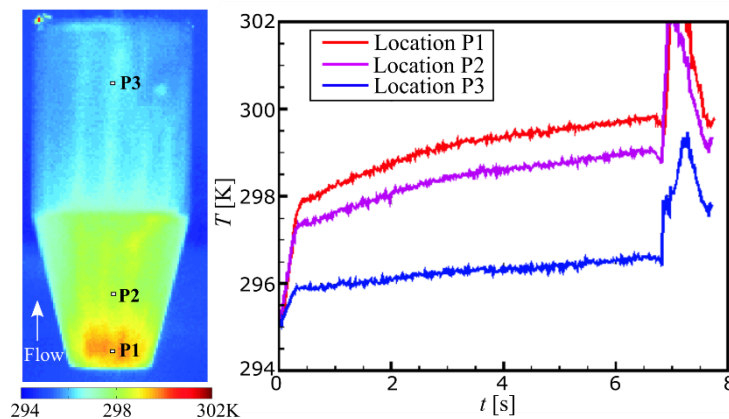


FIG. 2: (Color online) Windward view surface temperature profile of the truncated cone 1 at -12 degrees incidence angle. The left side figure shows the temperature map 3.5 s after wind tunnel start.

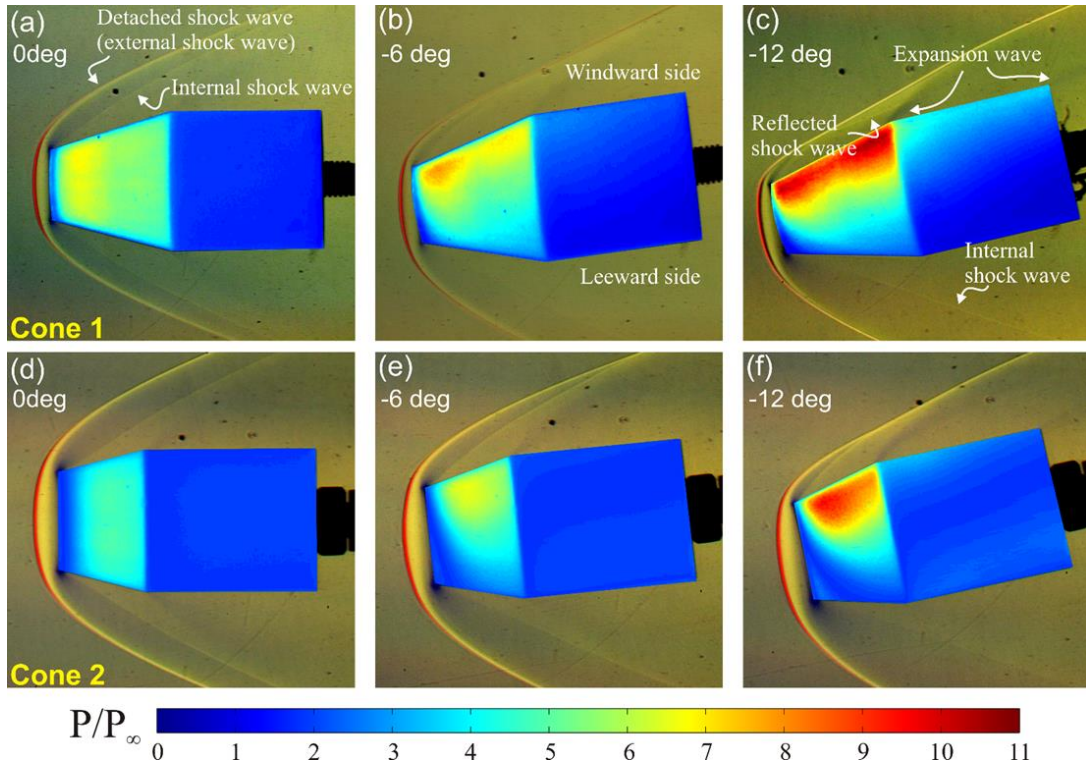


FIG. 3: (Color online) Side view colour schlieren/AA-PSP of the truncated cones.

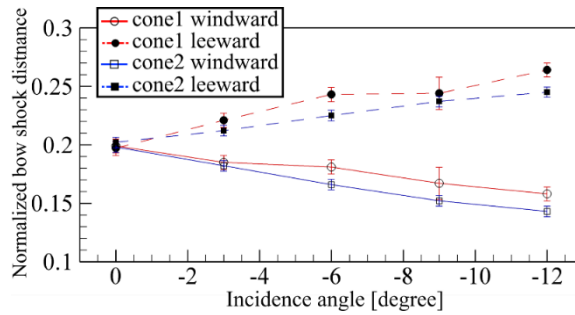


FIG. 4: (Color online) Normalized bow shock distances from the windward and leeward nose edges.

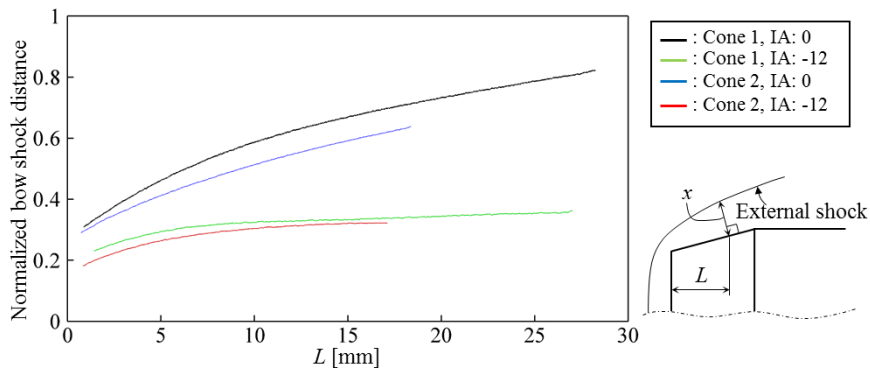


FIG. 5: (Color online) Normalized external shock distances on the conical surface.

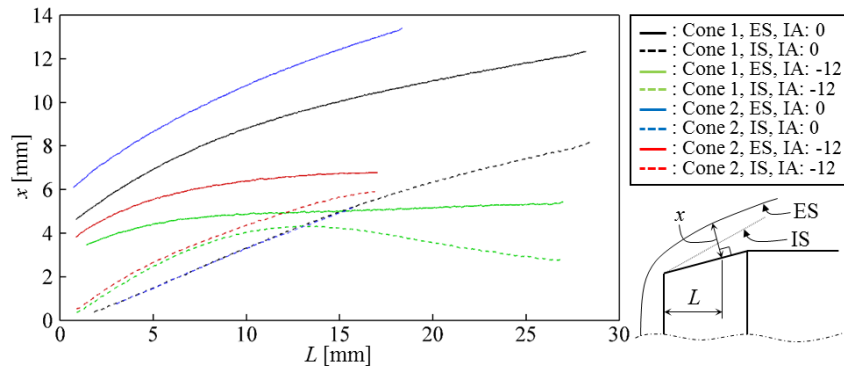


FIG. 6: (Color online) Distance between the shock waves and the model conical surface at 0 and -12 degrees incidence angles.

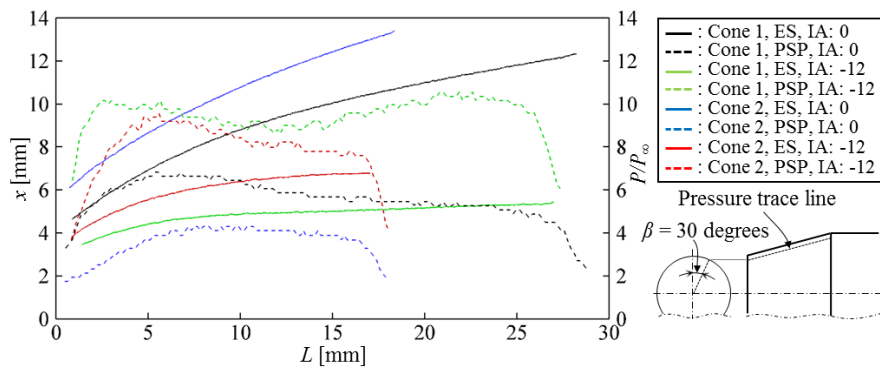


FIG. 7: (Color online) Comparison of the distance of the external shock waves and the surface pressure distribution.

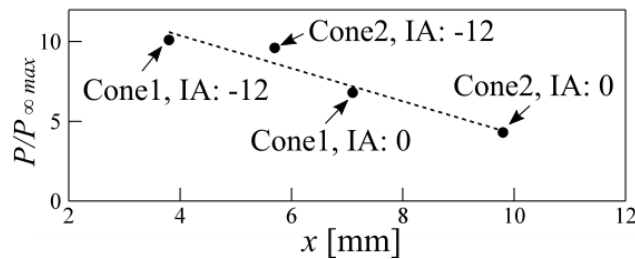


FIG. 8: Relation between maximum surface pressure and the distance of the external shock wave, the dashed line denotes approximate line.

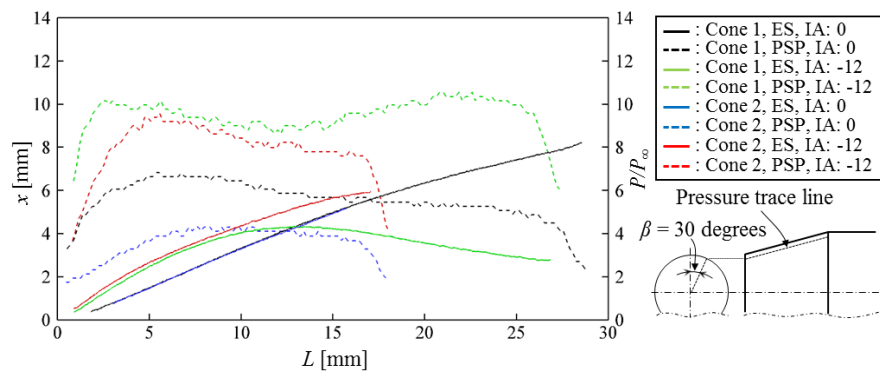
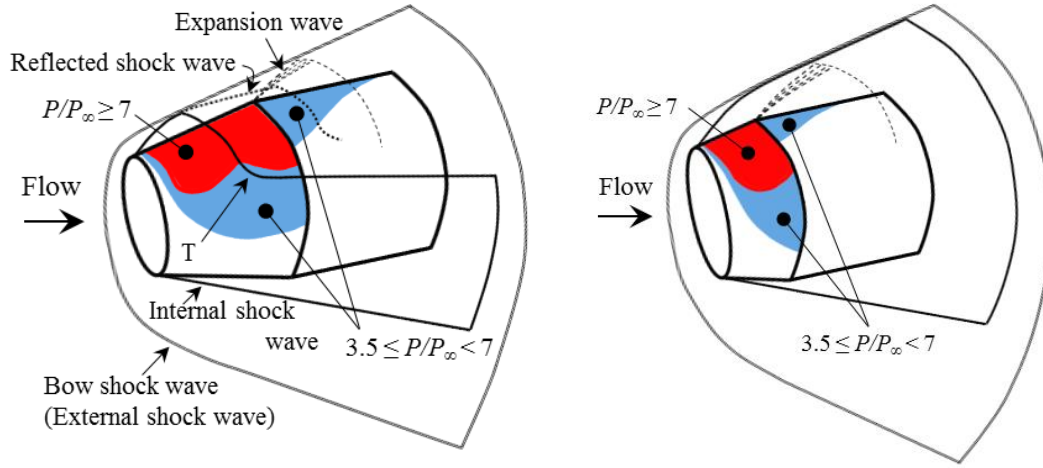


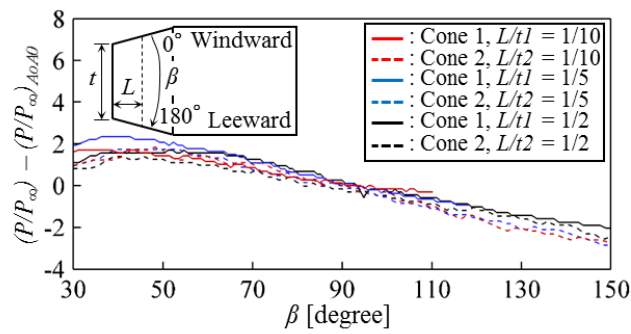
FIG. 9: (Color online) Comparison of the distance of the internal shock waves and the surface pressure distribution.



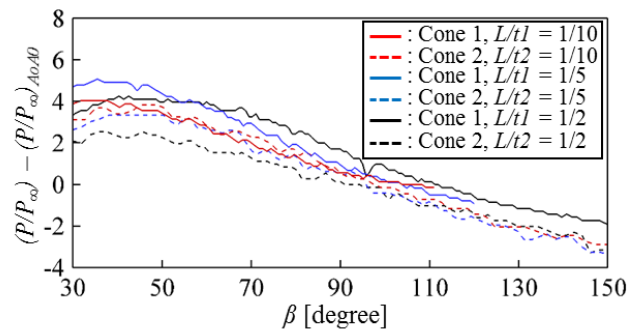
(a) Cone 1

(b) Cone 2

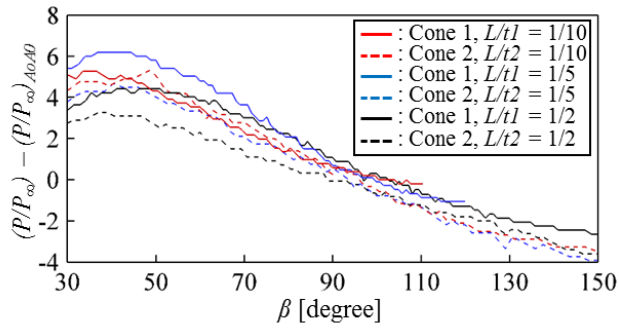
FIG. 10: (Color online) Three-dimensional flow field at -12 degrees incidence angle.



(a) -6 degrees



(b) -9 degrees



(c) -12 degrees

FIG. 11: (Color online) Circumferential surface pressure distribution at various incidence angles.

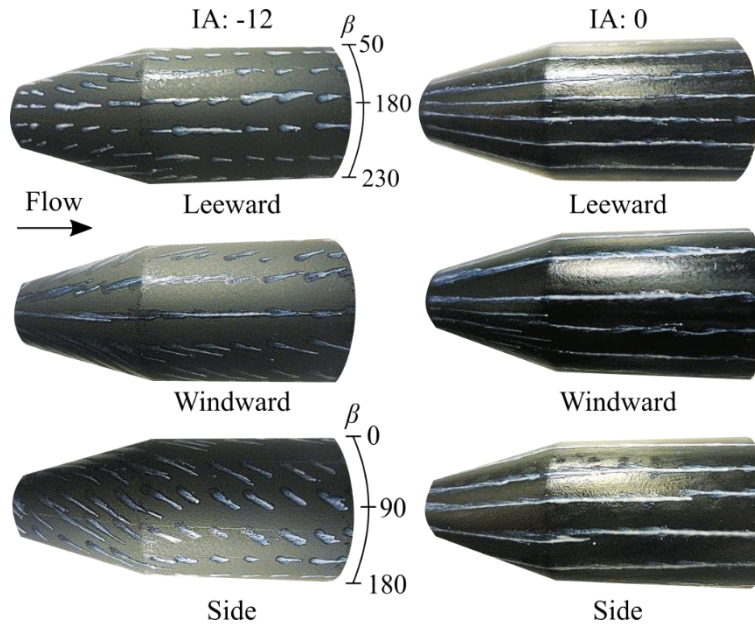


FIG. 12: Oil dot pattern on the truncated cone 1 at 0 and -12 degrees incidence angles and model orientations.

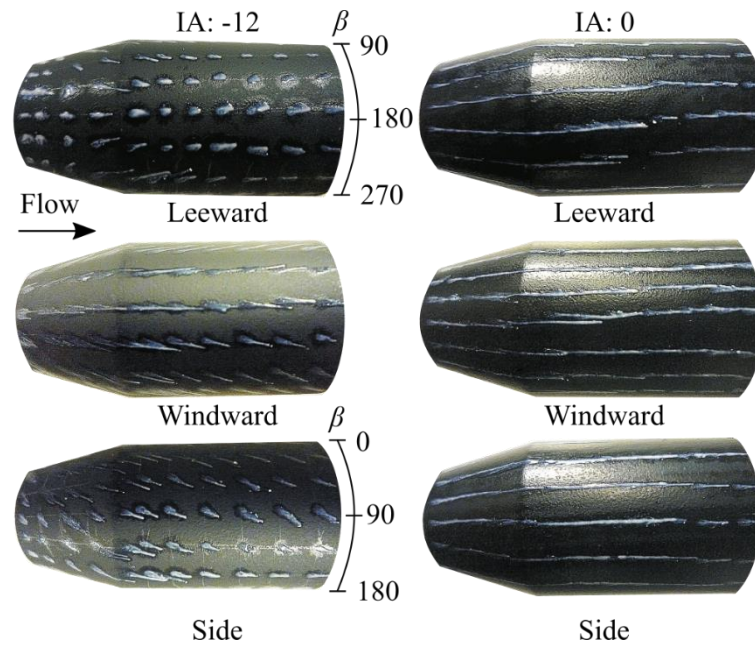


FIG. 13: Oil dot pattern on the truncated cone 2 at 0 and -12 degrees incidence angles and model orientations.

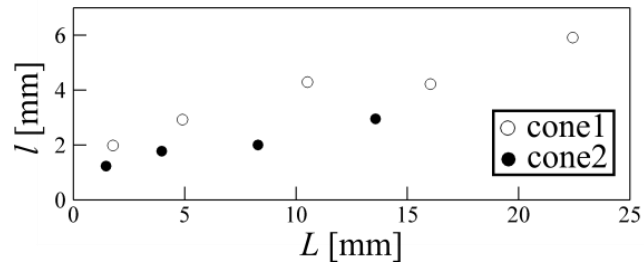
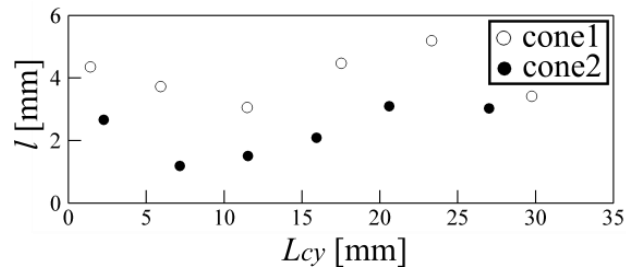
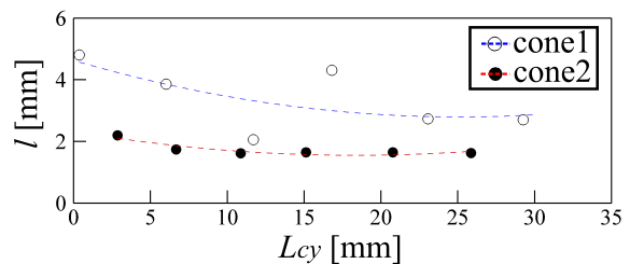


FIG 14: Oil streak length along approximately  $\beta = 180$  degrees on the leeward conical surface.



(a) Oil streak length along approximately  $\beta = 180$  degrees



(b) Oil streak length along approximately  $\beta = 150$  degrees

FIG 15: (Color online) Leeward view oil flow results on the cylindrical surface.

## Table

Table 1: Experimental conditions of AA-PSP on the truncated cone models.

Total pressure $P_o$ , kPa	645.9
Total temperature $T_o$ , K	372.3
Freestream Mach number $M_\infty$	5.0
Freestream pressure $P_\infty$ , kPa	1.22
Freestream temperature $T_\infty$ , K	62.5
Reynolds number $Re$	$3.8 \times 10^5$
Incidence angles $\alpha$ , degrees	-12 to 0 every 3 degrees